LAWRENCE
LIVERMORE
NATIONAL
LABORATORY

UCRL-TR-228340

Nonaqueous Phase Liquid Dissolution in Porous Media: Multi-Scale Effects of Multi-Component Dissolution Kinetics on Cleanup Time

Walt McNab, Souheil Ezzedine, Russ Detwiler

February 26, 2007

Disclaimer

This work performed under the auspices of the U.S. Department of Energy by Lawrence Livermore National Laboratory under Contract DE-AC52-07NA27344.

Nonaqueous Phase Liquid Dissolution in Porous Media: Multi-Scale Effects of Multi-Component Dissolution Kinetics on Cleanup Time

W. McNab
S. Ezzedine
R. Detwiler

Introduction

Industrial organic solvents such as trichloroethylene (TCE) and tetrachloroethylene (PCE) constitute a principal class of groundwater contaminants. Cleanup of groundwater plume source areas associated with these compounds is problematic, in part, because the compounds often exist in the subsurface as dense nonaqueous phase liquids (DNAPLs). Ganglia (or "blobs") of DNAPL serve as persistent sources of contaminants that are difficult to locate and remediate (e.g. Fenwick and Blunt, 1998). Current understanding of the physical and chemical processes associated with dissolution of DNAPLs in the subsurface is incomplete and yet is critical for evaluating long-term behavior of contaminant migration, groundwater cleanup, and the efficacy of source area cleanup technologies. As such, a goal of this project has been to contribute to this critical understanding by investigating the multi-phase, multi-component physics of DNAPL dissolution using state-of-the-art experimental and computational techniques. Through this research, we have explored efficient and accurate conceptual and numerical models for source-area contaminant transport that can be used to better inform the modeling of source area contaminants, including those at the LLNL Superfund sites, to re-evaluate existing remediation technologies, and to inspire or develop new remediation strategies.

The problem of DNAPL dissolution in natural porous media must be viewed in the context of several scales (Khachikian and Harmon, 2000), including the microscopic level at which capillary forces, viscous forces, and gravity/buoyancy forces are manifested at the scale of individual pores (Wilson and Conrad, 1984; Chatzis et al., 1988), the mesoscale where dissolution rates are strongly influenced by the local hydrodynamics, and the field-scale. Historically, the physico-chemical processes associated with DNAPL dissolution have been addressed through the use of lumped mass transfer coefficients which attempt to quantify the dissolution rate in response to local dissolved-phase concentrations distributed across the source area using a volume-averaging approach (Figure 1). The fundamental problem with the lumped mass transfer parameter is that its value is typically derived empirically through column-scale experiments that combine the effects of pore-scale flow, diffusion, and pore-scale geometry in a manner that does not provide a robust theoretical basis for upscaling.

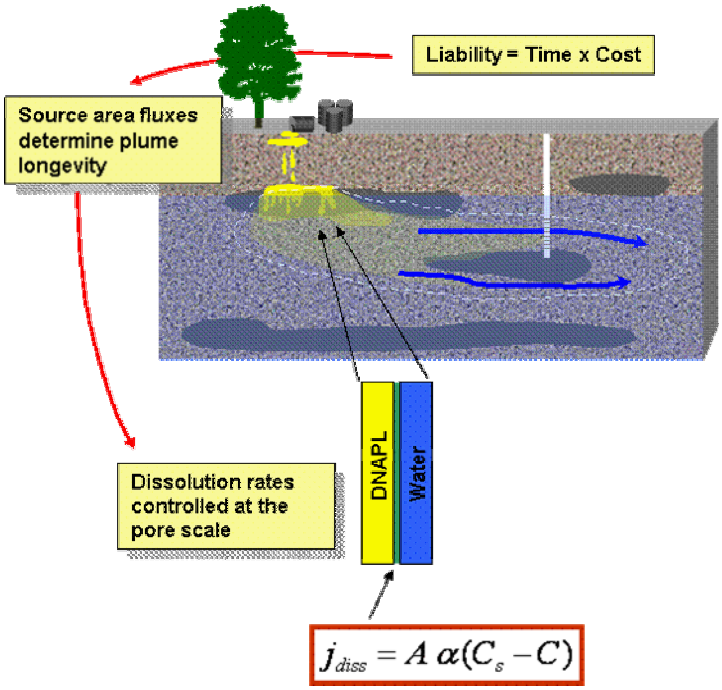

Figure 1. The longevity of groundwater contaminant plume emanating from DNAPL sources is ultimately determined by the rate of mass transfer across the DNAPL-water interface, j_{diss}, on a pore scale. This rate depends upon the interfacial area, A, the mass transfer coefficient, α, the solubility, C_s, and the aqueous concentration, C.

In our view, upscaling processes from the pore-scale to the field-scale requires new computational approaches (Held and Celia, 2001) that are directly linked to experimental studies of dissolution at the pore scale. As such, our investigation has been multi-pronged, combining theory, experiments, numerical modeling, new data analysis approaches, and a synthesis of previous studies (e.g. Glass et al, 2001; Keller et al., 2002) aimed at quantifying how the mechanisms controlling dissolution at the pore-scale control the long-term dissolution of source areas at larger scales.

Methods

Experimental Approach

The behavior of multi-phase fluid systems in two-dimensional analog porous media can be studied in detail by mating two pieces of textured glass together in the presence of a transmitted light source. The contact points between the two glass-plates represent the contact points between soil grains and the large gaps between the plates represent pores. This approach creates a two-dimensional analog porous medium that is more representative of pore-space geometry than typical micromodels constructed of a series of circular pore bodies connected by linear pore throats (e.g., Jia et al., 1999, Wan et al., 1996). This approach was initially developed to study fundamental single and two-phase flow and transport processes in fractures (e.g. Nicholl et al., 1999; Detwiler et al., 2000; 2001). Recently, it was used to investigate the effect of surfactants on DNAPL dissolution in porous media (Zhong et al., 2001).

Because the analog porous medium is transparent, light transmission techniques can be utilized to measure the pore-space geometry and the evolving geometry of entrapped DNAPL during dissolution. In our study, the analog porous medium was placed upon a uniform light source while a high-resolution (2048 x 3072 pixel) CCD camera accurately measured the intensity of transmitted light over the entire domain (Figure 2).

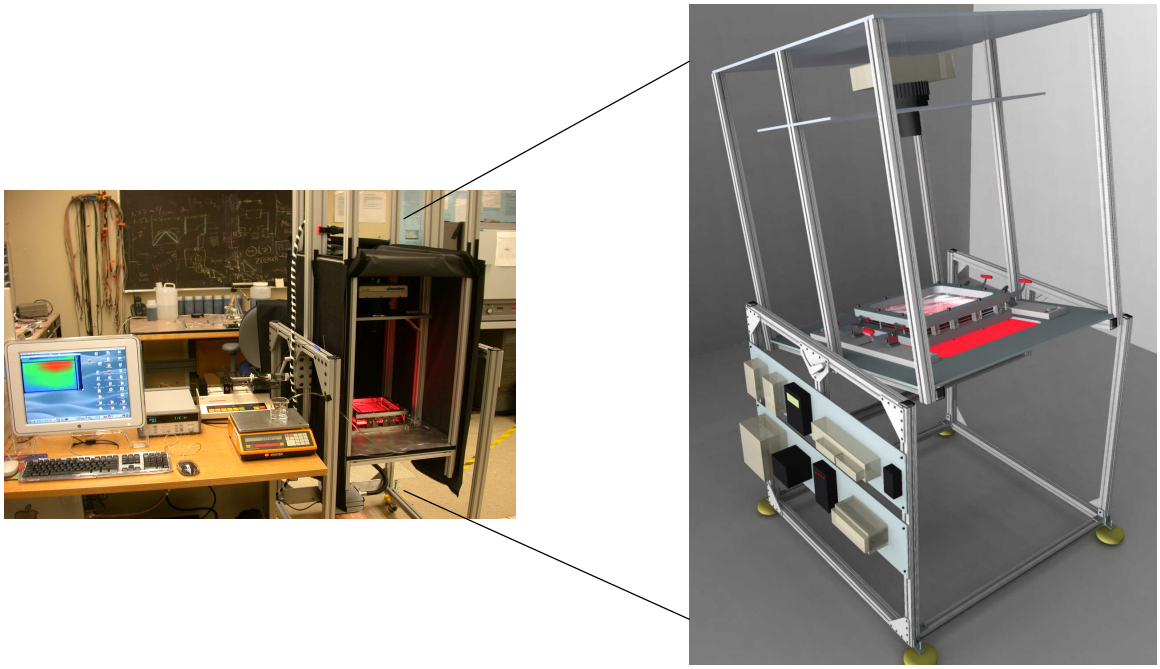

Figure 2. The experimental apparatus consists of a test stand that rigidly supports a steady, uniform light source and a high-resolution CCD camera. During the experiments, the rotating test stand is cloaked to block ambient stray light from interfering with CCD imaging. CCD camera is directly connected to a computer for image acquisition and processing.

The transmitted light can be directed through textured glass plates – representing different types of analog porous media (regular versus irregular, fractured, etc.) – or through two smooth glass plates, comprising the classic Hele-Shaw configuration (Figure 3).

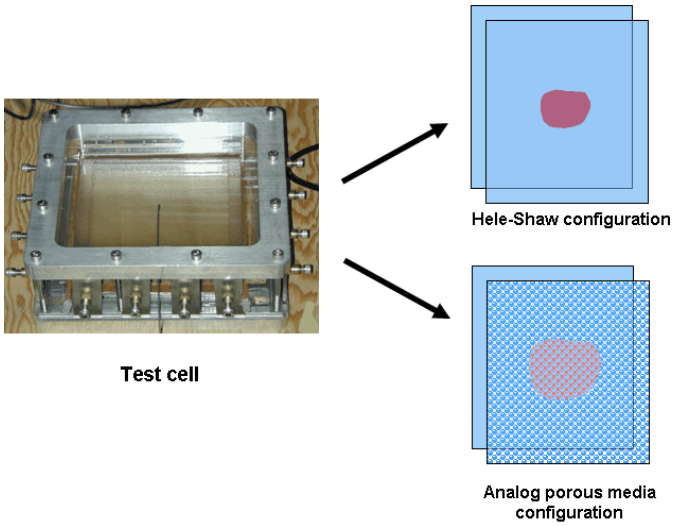

Figure 3. The test cell can be configured to represent analog 2-D porous media (using textured glass plates) or a Hele-Shaw cell (using smooth glass plates).

By sequentially filling the porous medium with a solution containing different concentrations of dye, for example, the space between the glass plates can be accurately quantified (±2 μm) with a lateral resolution of 150 x 150 μm or better, depending on the size of the samples (Detwiler et al., 1999), based on the Beer's law relationship:

$$I = I_0 e^{-\mu C b} \qquad \text{(Eq-1)}$$

where I is the transmitted light intensity, I_0 the light output of the source, μ the absorptivity of the solute, C the solute concentration, and b the length of the light path. Moreover, dying the water during dissolution experiments provides a contrast between the water and DNAPL, allowing the location of each DNAPL/water interface to be tracked over the duration of a dissolution experiment (Figure 4). Measurements of both the pore-space geometry and the evolving locations of DNAPL-water interfaces allow the calculation of the interfacial area of each DNAPL ganglion as a function of time. Such detailed measurements are critical to the understanding of the pore-scale interaction of hydrodynamics and mass transfer rates.

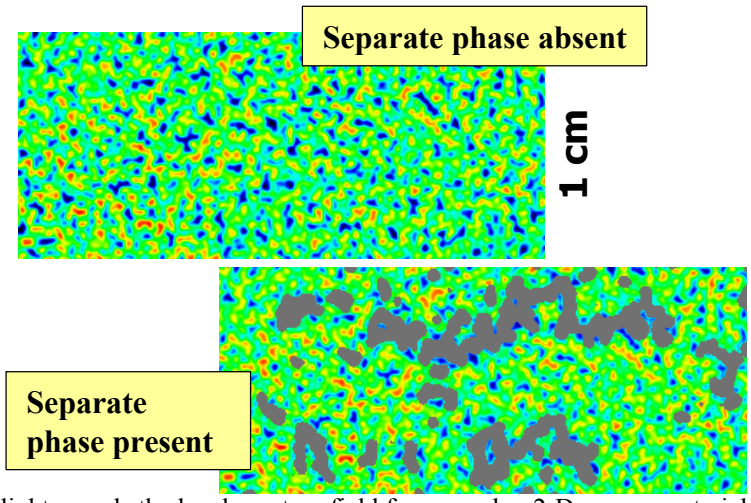

Figure 4. Transmitted light reveals the local aperture field for an analog 2-D porous material as well as the presence of separate phase fluids (CO_2 bubbles in this example test image).

Modeling Approach

The defining macroscopic characteristic of a plume source area is the change in concentration that occurs downgradient of the source area. This change is a result of the heterogeneous chemical reaction (DNAPL dissolution) that occurs across the distributed DNAPL-water interface (Figure 5). Accurate modeling of the source area requires that rate of dissolution at the micro-scale be accurately transformed through several length scales to the field-scale. This scaling issue is pivotal in developing large-scale descriptions of DNAPL dissolution that are built upon the underlying microscopic processes as a foundation. Most existing groundwater contaminant models bypass this step, leading to inconsistencies between the hierarchies. Our approach is to employ a more consistent modeling formulation.

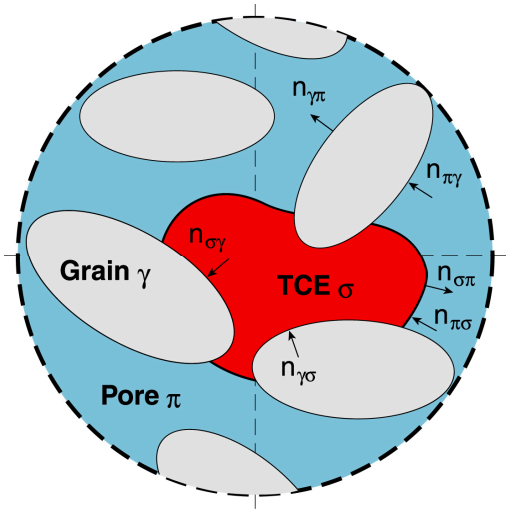

Figure 5. Physio-chemical domains to be considered in pore-scale DNAPL dissolution.

Single-phase flow modeling in porous media entails the use of volume-averaged flow and transport equations on the macroscopic scale. However, on the microscopic scale (in both

single- and multi-phase systems), the velocity field in the pore space is governed by Stokes' equations:

$$\mu_\pi \nabla^2 v_\pi + \rho_\pi g - \nabla p_\pi = 0 \qquad \text{(Eq.-2, in } \pi\text{-phase)}$$

$$\nabla \cdot v_\pi = 0 \qquad \text{(Eq.-3, in } \pi\text{-phase)}$$

$$v_{\pi\gamma} \cdot v_\pi = 0 \qquad \text{(Eq.-4, at the } \pi - \gamma \text{ interface)}$$

where p_π, ρ_π, μ_π, v_π, are the total pressure, total mass density, coefficient of viscosity, and mass average velocity in the π-phase, respectively, and g the gravitational acceleration constant (Figure 5). Most porous media of practical importance are hierarchical in nature, i.e., they are characterized by more than one length scale. When these length scales are disparate, the hierarchical structure can be analyzed by the method of volume averaging (i.e., Gray et al., 1993), leading to Darcy's law and the volume averaged continuity equation:

$$\langle v_\pi \rangle = -\frac{K_\pi}{\mu_\pi}\left(\nabla \langle p_\pi \rangle^\pi - \rho_\pi g\right) \qquad \text{(Eq.-5)}$$

$$\nabla \cdot \langle v_\pi \rangle = 0 \qquad \text{(Eq.-6)}$$

where $\langle v_\pi \rangle$, K_π, $\langle p_\pi \rangle^\pi$ are the superficial volume average velocity, Darcy's permeability tensor, and intrinsic average pressure in the π-phase, respectively. The transport of contaminants at the microscopic level is described by the following equations and conditions:

$$\frac{\partial c_\pi}{\partial t} + \nabla \cdot \left(v_\pi c_\pi - D \nabla c_\pi\right) = 0 \qquad \text{(Eq.-7, in the } \pi\text{-phase)}$$

$$c_\pi = F(c_\pi, c_\pi^{eq} k, t, \ldots) \qquad \text{(Eq.-8, at the } \pi\text{-}\sigma \text{ interface)}$$

$$c_\pi (v_\pi - w) \cdot n_{\pi\sigma} = -c_\sigma^0 w \cdot n_{\pi\sigma} \qquad \text{(Eq.-9, at the } \pi\text{-}\sigma \text{ interface)}$$

$$c_\pi (v_\pi - w) \cdot n_{\pi\gamma} = 0 \qquad \text{(Eq.-10, at the } \pi\text{-}\gamma \text{ interface)}$$

$$v_\sigma \cdot n_{\pi\sigma} = 0 \qquad \text{(Eq.-11, at the } \pi\text{-}\sigma \text{ interface)}$$

where c_π is the molar concentration in the π-phase, v_π the velocity in the π-phase, c_π^{eq} the equilibrium concentration in the π-phase, w the speed of displacement of the σ-π interface, c_σ°, the molar concentration of pure species, and v_σ the velocity in the σ. $n_{\pi\sigma}$ and $n_{\pi\gamma}$, refer to the unit

normal vector directed from the π-phase toward the α-phase (α=σ, γ), respectively. *D* is the mixture molecular diffusivity. The term $F(c_\pi, c_\pi^{eq}, k, t,)$ is in general a non-linear function of c_π, dissolution reaction rates, time, etc., is the driving-force term representing the dissolution kinetics of DNAPL (σ-phase) in the water (π-phase).

The system of coupled flow and transport equations has been solved numerically in this study by employing a Galerkin finite element approach as implemented by FlexPDE, a commercial product that solves partial differential equations (PDEs) with a highly sophisticated, state-of-the art adaptive grid methodology (featuring automatic mesh refinement, or AMR). With FlexPDE (originally developed at Lawrence Livermore National Laboratory), PDEs are directly scripted and then are parsed, linearized through a Newton-Raphson scheme, and solved using a variety of robust numerical techniques. The FlexPDE code has been validated on numerous published problems and is used by thousands of individuals and adopted by universities around the world.

A test problem example involving the simulation of the dissolution of two DNAPL blobs in a hypothetical two-dimensional medium (i.e., a Hele-Shaw cell) using the governing system of equations as formulated in FlexPDE is shown on Figure 6.

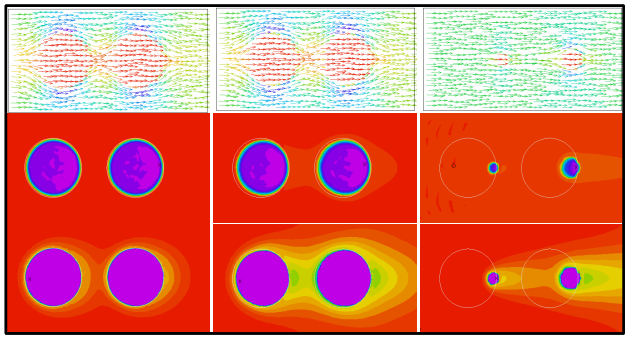

Figure 6: Numerical simulation of two DNAPL blobs dissolving in initially pure water. The first column depicts the velocity field, DNAPL, and dissolved-phase initial conditions (from top to bottom, respectively). The second column shows corresponding snapshots of the system at some intermediate time. The third column shows the response of the velocity field to changes in the sizes of the blobs, as well as the effect of the upgradient blob on the dissolution of the downgradient blob, at a still-later time.

Pore-Scale Experimental and Modeling Results: Selected Examples

CO_2 dissolution at the pore scale

CO_2 gas provided a useful surrogate for DNAPL during development and evaluation of the experimental apparatus because it dissolves rapidly in water and poses no significant ES&H hazards. As a test case, CO_2 dissolution experiments were conducted in flowing water between two smooth parallel plates. The purpose of the experiment was to collect a series of images of the blob during dissolution, transfer the digitized images of the position of the water-CO_2 ("DNAPL") interface as a function of time to the numerical model, and then evaluate the coupled model (interface position + dynamic Navier-Stokes-described flow field surrounding the blob) by comparing model output to the data from the experiment. Simulation results and observations are in good agreement (Figure 7). The resulting mass transfer relationships gleaned from the simulation results are shown on Figure 8.

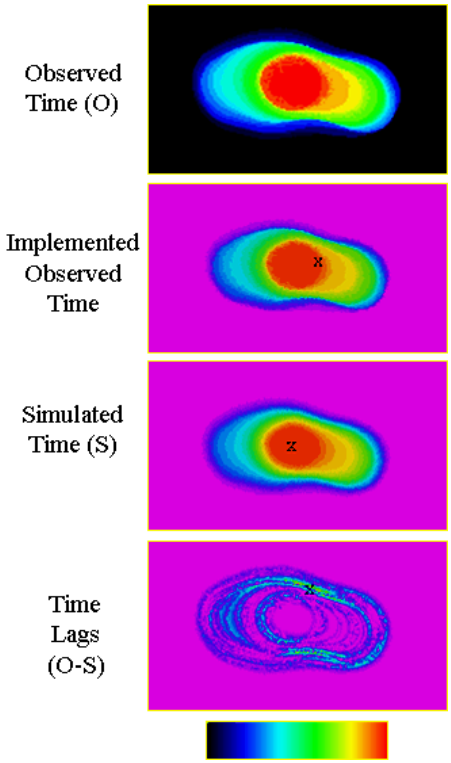

Figure 7. Dissolution of CO_2 gas blob (scale of the blob is on the order of 1 cm) in a Hele-Shaw cell filled with flowing water: a) observed interface at different times, as indicated by color shading (top), b) position of interface as digitally implemented in the numerical model, c) simulated interface as a function of time, and d) difference between the observed and simulated cases.

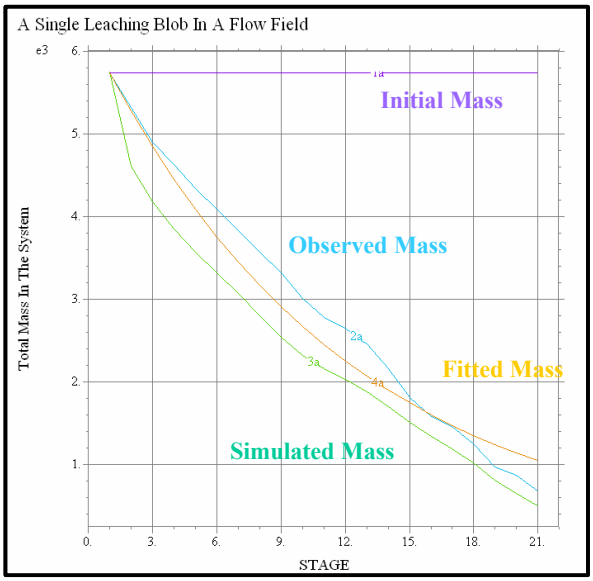

Figure 8. Observed, simulated, and fitted mass transfer rates time. Each stage lasted 4 hours with a flow rate of 0.4ml/min through the test cell. The effective mass transfer rate for the blob was computed as $\alpha = 0.34\ h^{-1}$.

The CO_2 blob dissolution test case can be readily extended to a second (hypothetical) example involving the dissolution of *supercritical* CO_2, a key problem in the injection of waste CO_2 from fossil fuel power plants as a means for combating global warming. Supercritical CO_2, a fluid phase separate from that of ordinary gas or liquid, forms above 73.8 bar and 31.1°C in *P-T* parameter space, conditions that could not be achieved with our experimental apparatus. Nevertheless, dissolution of a supercritical CO_2 blob is illustrative for computational physics purposes because it involves the phenomenon of Saffman-Taylor instability. This type of flow instability occurs when a low viscosity fluid (supercritical CO_2) is injected into a more viscous one (water), leading to a viscous fingering effect. Specifically, Saffman-Taylor instability occurs above a threshold value, *U,* given by,

$$U < \frac{(\rho_2 - \rho_1) g k \cos(\theta)}{(\mu_2 - \mu_2)\phi} \qquad \text{(Eq.-12)}$$

where ρ_1, ρ_2, μ_1, and μ_2 are the respective densities and viscosities of the two fluids, g the gravitational acceleration constant, *k* the permeability of the medium, θ the angle of the normal vector to the interface with the direction of gravity, and φ the porosity (Phillips, 1991). Simulation results using the coupled numerical model employing the properties of supercritical CO_2 as a separate phase fluid, over a similar spatial scale to the CO_2 gas bubble dissolution experiment, are shown on Figure 9 for a vertically-oriented flow domain. The model is clearly successful at reproducing the fingering effect, illustrating the capability of the coupled equations as implemented in FlexPDE to capture the essential physics of the problem.

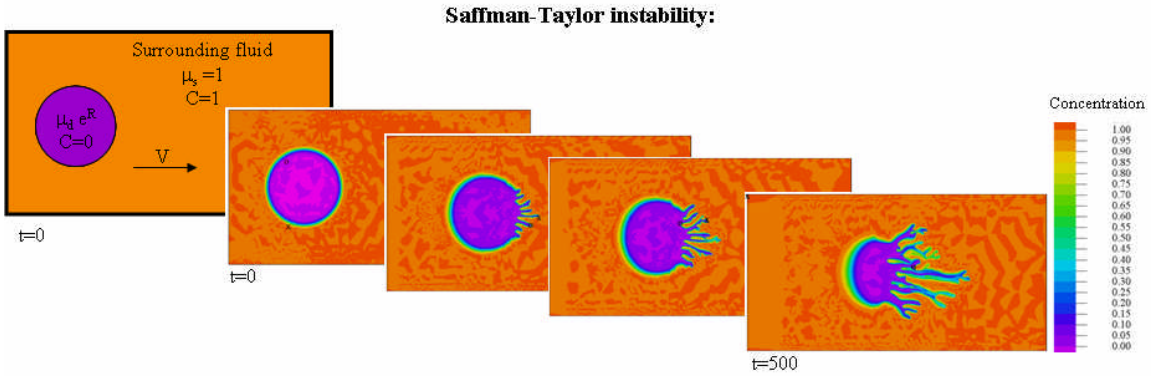

Figure 9. Simulation of the dissolution of a supercritical CO_2 blob in a hypothetical Hele-Shaw cell.

TCE dissolution at the pore scale

A series of TCE DNAPL dissolution experiments was conducted in a Hele-Shaw test cell configuration for the purpose of quantifying an intrinsic mass transfer coefficient under conditions of controlled geometry and flow at the pore scale (and thus in contrast to the lumped mass transfer coefficients measured in column experiments as reported in the literature). Specifically, the dissolution of a TCE blob was evaluated over five experimental stages, with the ambient water flow rate doubled between each stage. The dissolution of TCE DNAPL blob was imaged every two hours, yielding a total of 239 CCD images. Superposition of the images

allowed the evolution of the water-DNAPL interface to be evaluated with time (Figure 10) using a procedure analogous to that used for the initial CO_2 bubble dissolution test case.

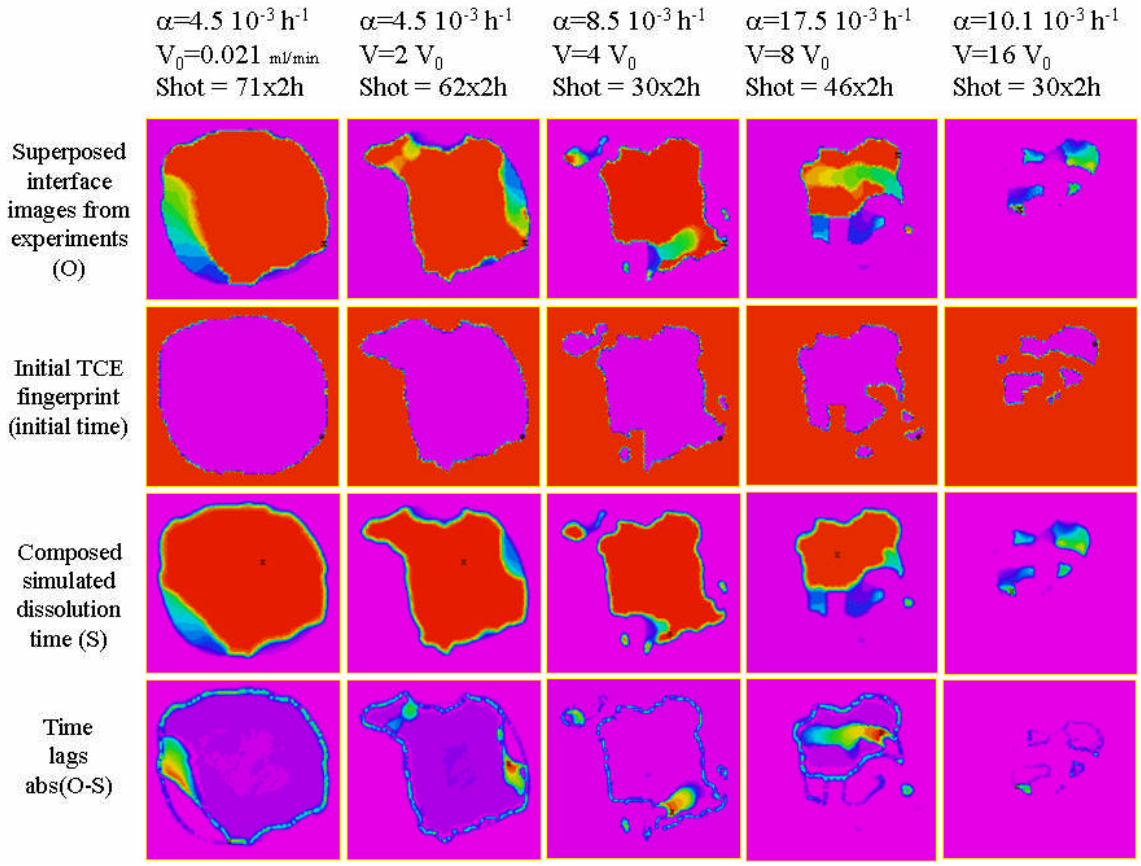

Figure 10. Composed TCE DNAPL-water interface shrinkage over time; experimental and numerical simulation resuts at different stages (1 through 5): a) observed interface morphology at different times (blue for early times, red for later times, top), b) initial TCE blob configuration as an initial condition for simulation, c) simulated interface evolution, and d) difference between the observed and simulated DNAPL interface shrinkage time. Simulations and observations are in very agreement, indicating that the dynamic updating of the Navier-Stokes-described flow field produces physically reasonable results in terms of the erosion patterns of the DNAPL blob.

After mass transfer coefficients for the TCE blob were computed for different stages, an intrinsic mass transfer coefficient for the interface, κ, was estimated for each stage using a velocity-weighting averaging scheme based upon the expression:

$$\kappa = \frac{\int_{\Gamma} \alpha v d\Gamma}{\Gamma \delta \int_{\Gamma} v^{*} d\Gamma} \qquad \text{(Eq.-13)}$$

where Γ is the surface of the DNAPL blob (obtained by pixel counting), α the mass transfer coefficient of the DNAPL blob, δ the test cell thickness, v^* the mean water velocity through the test cell, and v the local water velocity along the DNAPL-water interface. While the latter quantity could not be measured directly in the experiment, the good agreement between the

experimental and numerical results allowed *v* to be *computed* from the Navier-Stokes-described flow field (Figure 11).

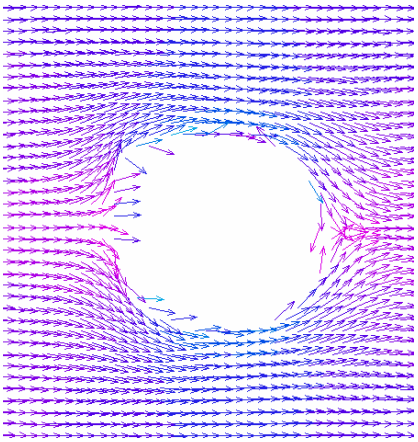

Figure 11. Computed Navier-Stokes-described local flow field surrounding a dissolving TCE DNAPL blob.

The resulting estimated interface intrinsic mass transfer coefficients (Table 1) exhibit less variability than the overall DNAPL blob mass transfer coefficients (the α-parameter values shown on Figure 10), despite changing flow rates.

Table 1. Estimated intrinsic mass transfer rate across the DNAPL/water interface

Stage	**Velocity**	**κ (mm^{-2} hr^{-1})**
1	V_0	1.02×10^{-5}
2	$2V_0$	1.03×10^{-5}
3	$4V_0$	1.41×10^{-5}

Numerical construction of synthetic periodic porous media and upscaling

Three-dimensional models of synthetic porous media that are packed according to various geometries (Figure 12) were developed to assist in upscaling mass transfer coefficients estimated from pore scale experiments and models. Each class of synthetic porous media was developed in such a manner as to honor prescribed probability distribution functions for grain size and the spatial correlations of grain size and geometrical constraints such as the grain-to-grain contact coordination number. In addition, to facilitate flow and transport modeling, blocks of synthetic porous media were designed to accommodate periodic, or "wrap-around," boundary condition constraint.

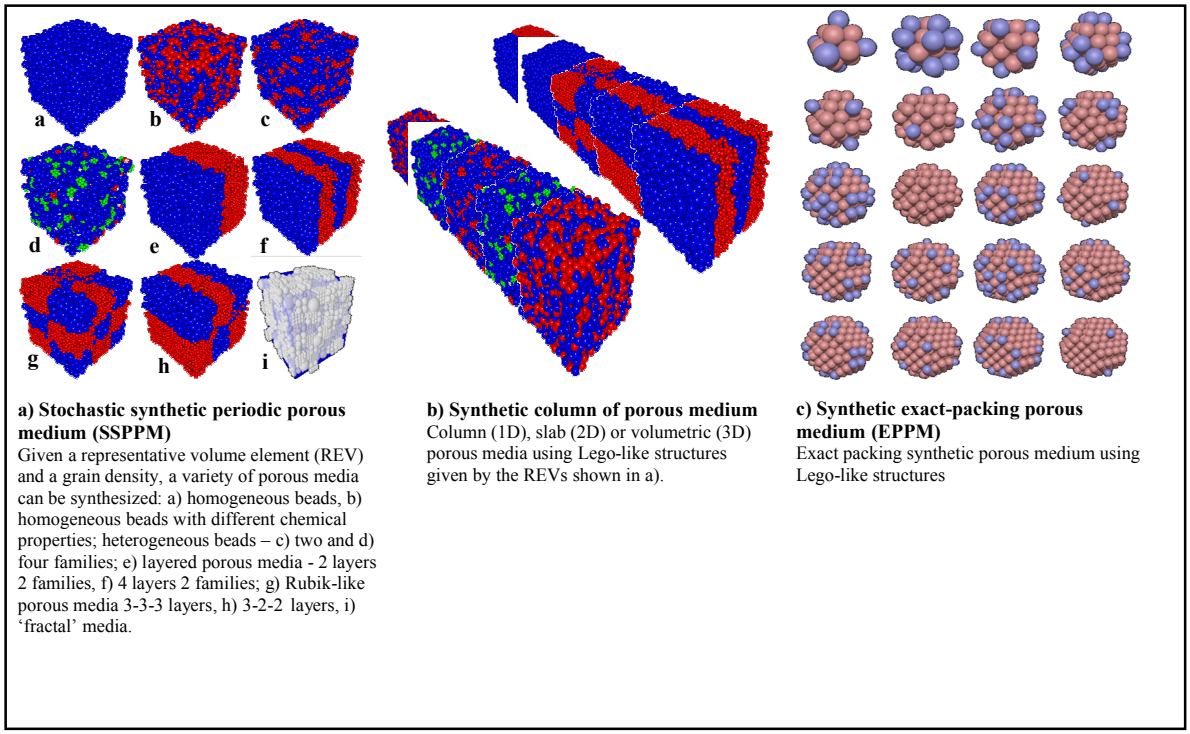

a) Stochastic synthetic periodic porous medium (SSPPM)
Given a representative volume element (REV) and a grain density, a variety of porous media can be synthesized: a) homogeneous beads, b) homogeneous beads with different chemical properties; heterogeneous beads – c) two and d) four families; e) layered porous media - 2 layers 2 families, f) 4 layers 2 families; g) Rubik-like porous media 3-3-3 layers, h) 3-2-2 layers, i) 'fractal' media.

b) Synthetic column of porous medium
Column (1D), slab (2D) or volumetric (3D) porous media using Lego-like structures given by the REVs shown in a).

c) Synthetic exact-packing porous medium (EPPM)
Exact packing synthetic porous medium using Lego-like structures

Figure 12. Synthetic deterministic exact-packing and stochastic porous media.

To construct and solve the pertinent coupled flow and transport equations for the 3-D synthetic porous media, grain/pore space geometry was discretized using immersed boundary techniques. AMR facilitated mesh refinement at the interfaces and, in particular, permitted better definition of small throat pore spaces that critically affect flow. An example of the resulting distribution of pressure and velocity in the pore space field obtained by solving the Navier-Stokes system of equations, using Livermore high performance computing resources, is shown on Figure 13.

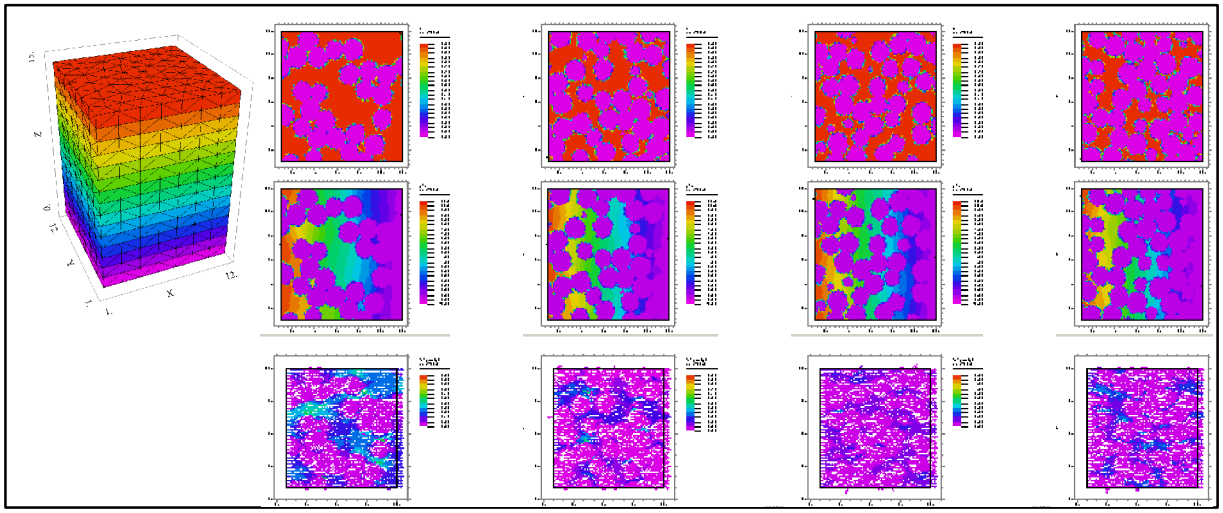

Figure 13. Vertical slices cut through a synthetic 3-D porous medium, showing the pore space, the pressure field and the velocity field.

Using different porous media packing schemes, it is possible to determine an upscaled effective mass transfer coefficient by relating the proportion of the remaining DNAPL mass to the ratio of the average mean dissolved concentration in the system and the solubility limit of the DNAPL. Moreover, by changing only the diameter of the soil grains in deterministic synthetic porous packing, it is also possible to assess the role of the morphology of the pore space and entrapped DNAPL on the hydrodynamics and the dissolution of DNAPL. To test this concept, the flow and transport model was applied to a series of different EPPM (as defined on Figure 12). Boundary head conditions were distributed as shown on Figure 14a; to check the validity and the consistency of the numerical solution, these boundary conditions were applied to each of the six faces of the porous media block.

The overall purpose of the upscaled simulations is to effectively describe DNAPL dissolution in the porous media with an equivalent mass transfer flux source term for which the kinetics follows a rate-limited dissolution: flux = $-\alpha_{eff}(C_S - C_{av})$, where α_{eff} is the effective mass transfer coefficient, C_S is the solubility limit of DNAPL, and C_{av} is the average dissolved concentration in the porous media. Dimensional analysis implies that $\alpha_{eff} = a_0 (q/K)^a (M/M_0)^b$, where a_0, a and b are model parameters, q the mean Darcy velocity, K the effective saturated hydraulic conductivity, M_0 the initial DNAPL mass, and M is the current non-dissolved mass. This conceptualization is applicable to mesoscale porous media. To adopt it for the packed synthetic porous media, two alterations have been implemented. First, the hydraulic conductivity is replaced by its geometric counterpart $K = k\, n/g \sim d_{av}^2\, n/g$, where d_{av} is the average diameter of solid grain. Second, the average Darcy velocity is replaced by the magnitude of the average Stokes velocity with the porous media. In addition, a_0 was estimated using the Hele-Shaw experiments and simulations. The surface area of DNAPL was also computed during simulations.

The relationship between M/M_0 and C/C_S for all simulations (i.e., multiple realizations of pore geometry) is presented on Figure 14b. Numerical results indicate good agreement between the flow and transport cases (a strong central tendency) which further validates the numerical code. From prior published results, a was assumed equal to 1.0, leaving b as is the sole meso-scale model parameter to be estimated using non-linear regression methods. As such, the parameter b was estimated from regression to be equal to a value of approximately 0.392 with a variance of 1.2%. Similar numerical simulations were conducted for exact packing porous media with different grain diameters; these results are given on Figure 14c. The resulting relationship between the model parameter b with diameter d/d_0 is plotted on Figure 14d. This proposed model thus permits the selection of the appropriate model, given an average grain size diameter.

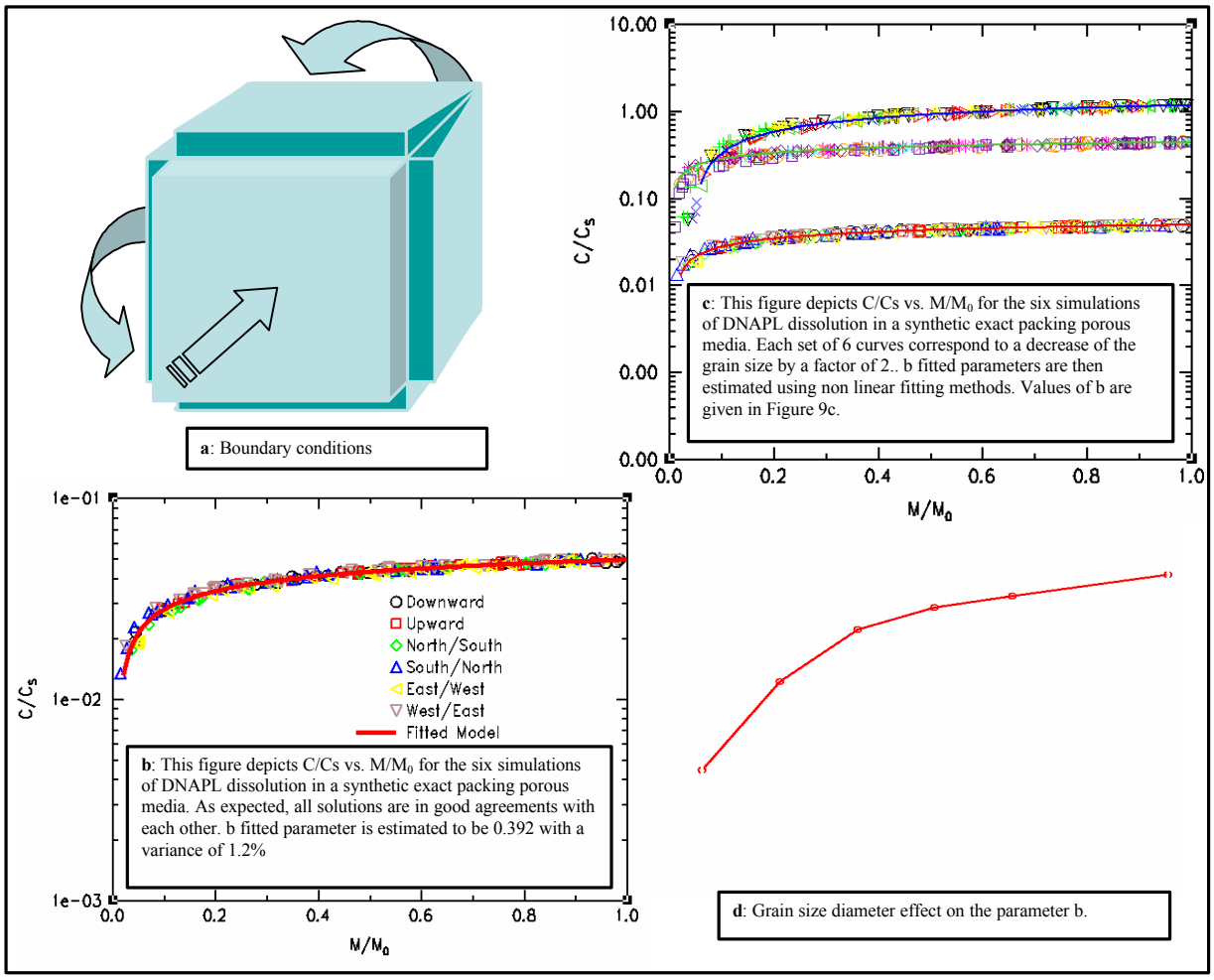

Figure 14. Effective source area model for synthetic deterministic exact-packing porous media.

Some Implications of the Intrinsic Mass Transfer Coefficient for TCE: Selected Examples

Enhanced TCE dissolution with KMnO4

In situ chemical oxidation is a remedial strategy that entails the injection of an oxidizing agent into the subsurface to bring about the destruction of contaminant mass in chlorinated hydrocarbon plume source areas. Permanganate ion, usually delivered in the form of dissolved $KMnO_4$, is a preferred oxidant because it reacts rapidly with TCE and other common organic contaminants. The oxidation of TCE by MnO_4^- yields Mn^{2+} ion as a reaction product:

$$C_2HCl_3 + MnO_4^- + H^+ \rightarrow 2CO_2 + 1.2Mn^{2+} + +3Cl^- + 0.8H_2O \qquad \text{(Eq.-14)}$$

In turn, Mn^{2+} can react with MnO_4^- to form solid phase MnO_2 precipitate:

$$0.4MnO_4^- + 0.6Mn^{2+} + 0.4H_2O \rightarrow MnO_2 + 0.8H^+ \qquad \text{(Eq.-15)}$$

As the aquifer pore spaces become clogged over time with MnO_2 precipitate, a reduction in hydraulic conductivity ensues, significantly affecting further source area remediation. To study this phenomenon on the pore scale, a two-dimensional analog porous media experiment was constructed using textured glass. As a first step, separate-phase TCE was injected into the test cell and flushed for a period of time with water (Figure 15). Next, a $KMnO_4$ solution was injected into the cell at a concentration of approximately 0.1 M. False-color CCD images of the experiment were generated, based on light attenuation, that depicted the configuration of the TCE ganglia as well as the deposition of light-absorbing material in the open aperture spaces that indicate Mn-bearing mineral phase deposition (Figure 16).

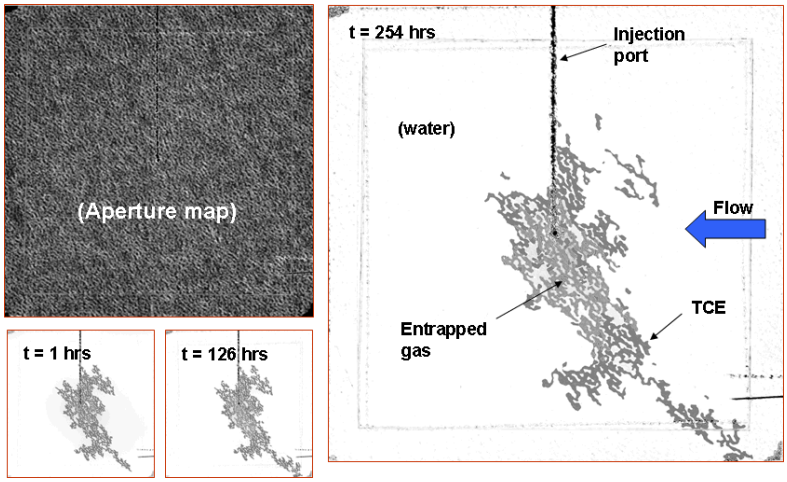

Figure 15. Images of TCE DNAPL ganglia distributed within an analog 2-D porous medium test cell.

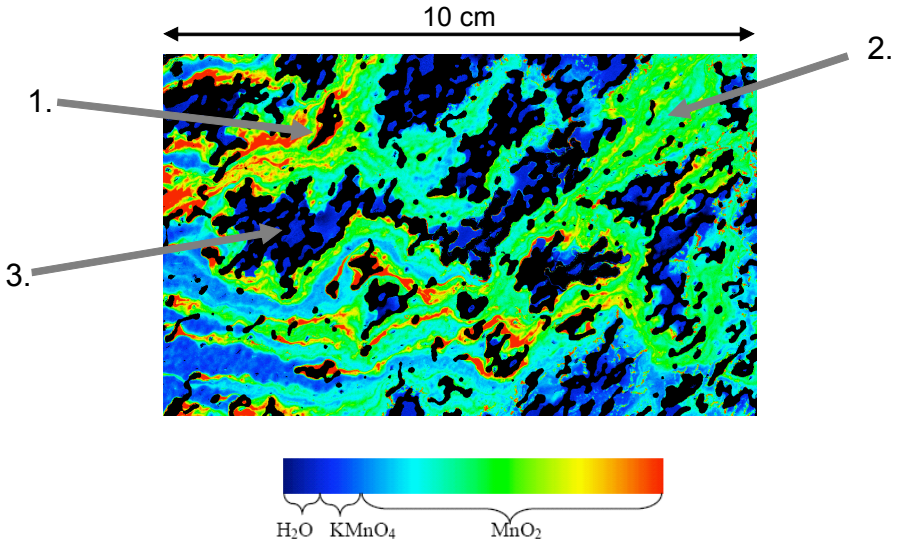

Figure 16. False-color image of an analog porous media experiment involving the dissolution of TCE ganglia (indicated in black) and subsequent oxidation by MnO_4^- in the injected water stream. Much of the MnO_2 precipitate occurs at the upgradient end of the cell (left side), sometimes surrounding large TCE blobs (1). Toward the downgradient end of the cell, some MnO2 precipitation is still evident, although the TCE blobs in this region appear to be significantly reduced in size (2). Elsewhere in the cell, hydraulically isolated regions indicate no MnO_2 precipitation and little or no TCE dissolution (3).

Two related questions arise from the imaging experiment: (1) whether or not the observed patterns of both TCE droplet dissolution and MnO_2 precipitation are consistent with the intrinsic TCE DNAPL/water mass transfer rate estimated in this study for TCE dissolution in pure water, and (2) whether or not the formation of mineral rinds around the TCE DNAPL blobs interfere with subsequent blob dissolution. To address these questions, the reactive transport capability of the PHREEQC geochemical speciation model (Parkhurst and Appelo, 2002) was employed to simulate the system geochemistry. PHREEQC is a general-purpose geochemical model that simulate changes in aqueous chemistry and specified mineral assemblages in response to thermodynamic as well as kinetic relationships. One-dimensional reactive transport can be simulated by linking together a series of individual geochemical models as cells that are connected by specified flux terms. For this application, the reactive transport model was based on the assumption of steady-state plug flow (ignoring dispersion), with a flow rate and geometry that were consistent with the parameters of the experiment. The model was discretized into 30 volume elements, with 4 pore volumes passed through the modeled system over a period of one hour. Circular TCE blobs with a diameter of 5 mm were assumed to exist as a mineral phase with kinetically-specified dissolution within each cell as an initial condition. The intrinsic mass transfer coefficient developed in this study was employed in the kinetic expression, along with a published value for the kinetics of the oxidation of dissolved-phase TCE by MnO_4^- (Yan and Schwartz, 1999). MnO_2 precipitation was assumed to occur, via the reaction given by Eq.-15, whenever MnO_2 became locally thermodynamically supersaturated in the simulated cell solution.

The results of the reactive transport modeling are shown on Figure 17 for three scenarios. The baseline case (top figure) is based on the assumption that the TCE blobs dissolved according to the baseline mass transfer coefficient of $\kappa = 1.0 \times 10^{-5}$ mm^{-2} hr^{-1}, independent of the quantity of MnO_2 precipitated within each cell. This scenario resulted in complete dissolution of all of the TCE blobs within the passage of four pore volumes. The second case (middle figure) was based on the assumption that the rate of TCE DNAPL dissolution was proportionally reduced as the mass of MnO_2 precipitated within each cell approached that of the remaining DNAPL. To assess parameter sensitivity, the third case (bottom figure) is based on the assumption that the intrinsic mass transfer coefficient ($\kappa = 1.0 \times 10^{-6}$ mm^{-2} hr-1) is an order of magnitude less than that estimated in the prior Hele-Shaw TCE blob dissolution experiment. Among the three cases, only the scenario that assumes some encapsulation of the TCE blobs by MnO_2, and hence a reduction in the dissolution rate, produces good qualitative agreement with the experimental image. Specifically, this scenario suggests that the MnO2 precipitation is concentrated toward the upgradient end of the cell, but with some dissolution of the TCE blobs evident toward the downgradient end. This result suggests that encapsulation of TCE blobs in the field on the microscopic (pore) could present a significant issue in field application of MnO_4^-, possibly leading to an overestimate of remediation success owing to a subsequent reduction in dissolved-phase TCE (or, alternatively, beneficially isolating the source term via entombment on the microscopic level).

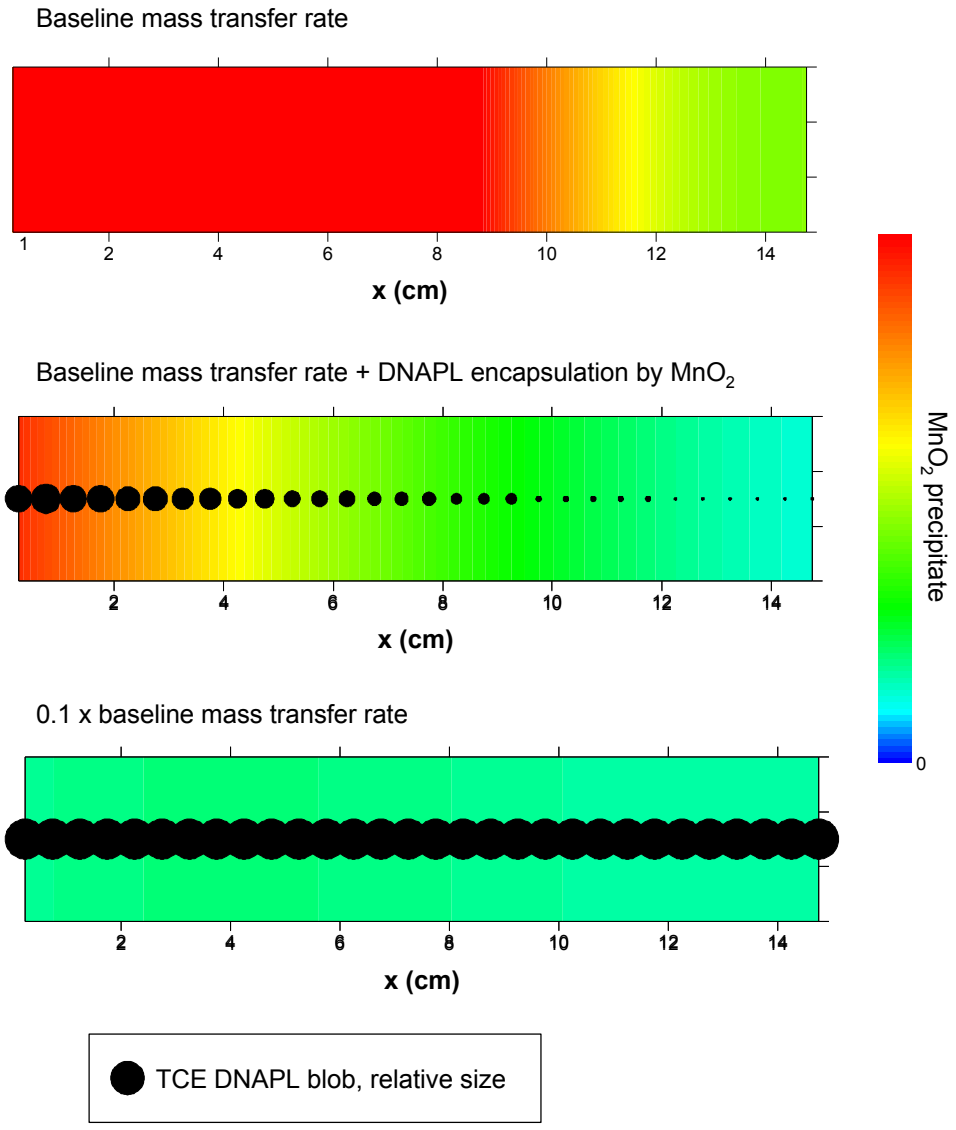

Figure 17. Relative sizes of TCE blobs and MnO2 precipitate as simulated by PHREEQC using the value of κ, the intrinsic TCE DNAPL/water mass transfer rate, estimated as part of this study. Flow direction is from left to right.

Plume longevity versus mass transfer coefficient

The impact of pore-scale-derived mass intrinsic mass transfer coefficient values on the overall longevity of groundwater contaminant plumes is a problematic question because uncertainties stemming from heterogeneities in the flow field emerge as the dominant issue at larger and large spatial scales. Nevertheless, a simplified modeling approach can be used to gain some insight into the *relative* importance of the mass transfer coefficient on source longevity compared to other factors such as mean groundwater velocity or source area geometry. For this effort, a two-component semi-analytical coupled source zone-plume model was developed that incorporates the intrinsic TCE DNAPL dissolution mass transfer coefficient estimated from Hele-Shaw cell laboratory experiments and pore-scale modeling.

The first component of the model is a simple mixed-tank reactor of a specified length, width, height, and porosity (presenting a source area "box" within an aquifer) containing a specified initial mass of DNAPL. The changes in mass of TCE per unit time in the dissolved phase within the source box, dM_w/dt, and within the DNAPL, dM_{DNAPL}/dt, are related by the two coupled ordinary differential equations:

$$\frac{dM_w}{dt} = \kappa\Gamma(M_{DNAPL})(C_s - \frac{M_W}{V}) - Q\frac{M_w}{V} \qquad \text{(Eq.-16)}$$

$$\frac{dM_{DNAPL}}{dt} = -\kappa\Gamma(M_{DNAPL})(C_s - \frac{M_W}{V}) \qquad \text{(Eq.-17)}$$

where κ is the intrinsic TCE DNAPL mass transfer coefficient (as quantified experimentally in this study), Γ surface area of the DNAPL mass (idealized as a population of *N*-spherical blobs), *V* the pore volume of the source box, and *Q* the volumetric flux of groundwater through the source box along its longitudinal axis.

The second model component is based upon an analytical solution to the advective-dispersive solute transport equation in an idealized uniform aquifer subject to an instantaneous point source release source term (Wilson and Miller, 1978). Here, the "slug" source model was modified by numerical integration of the time-dependent TCE solute flux emerging from the source box (as quantified by the first model component) to yield a plume model with a time-varying boundary condition that ultimately reflects the role of mass transfer within the source box on plume evolution:

$$C(x,y,t) = \int_0^t \frac{QC_0(t-\tau)}{4\pi\phi\tau b\sqrt{D_L D_T}} e^{-\frac{(x-v\tau)^2}{4D_L\tau} - \frac{y^2}{4D_T\tau}} d\tau \qquad \text{(Eq.-18)}$$

Both components of the model were solved for a variety of representative parameter settings using the MathCad computing platform (MathSoft, 2005). The results are summarized on Figures 18-21 and in Table 2.

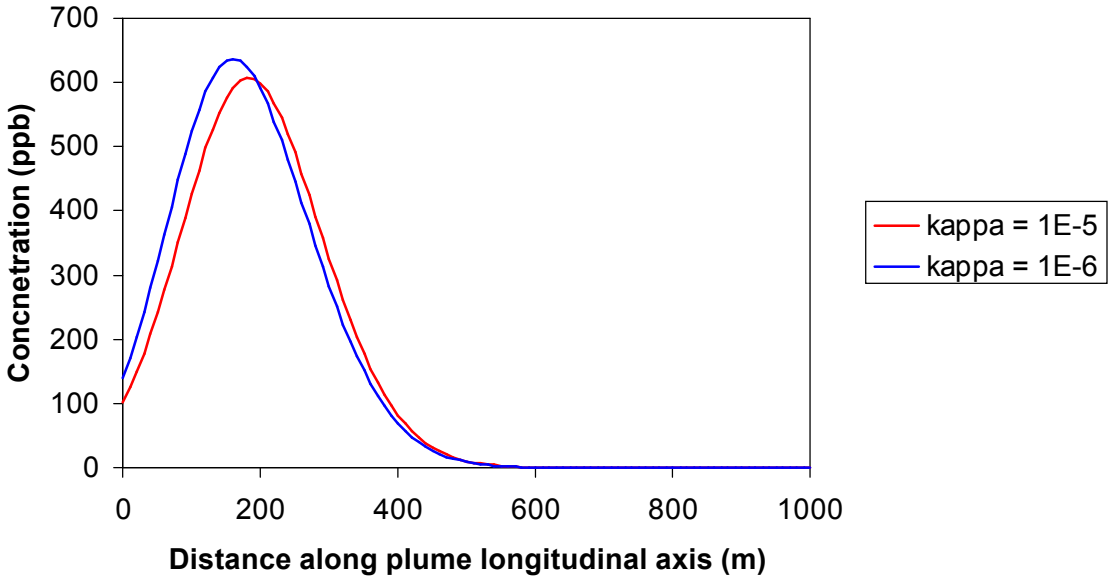

Figure 18. Longitudinal profiles of a groundwater TCE plume emanating from a 30-kg DNAPL source after 25 years for two values of the intrinsic interface mass transfer coefficient (mm^{-2} hr^{-1}). Pore velocity = 10 m/yr, DNAPL is distributed across N = 100 spherical blobs, and source box dimensions = 1 x 1 x 1 m.

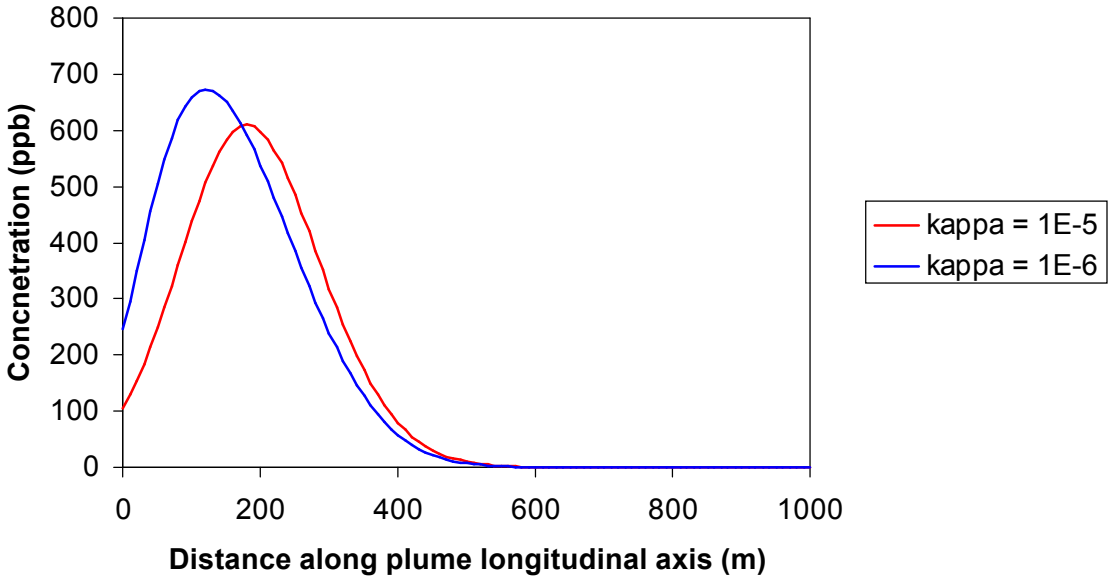

Figure 19. Longitudinal profiles of a groundwater TCE plume emanating from a 30-kg DNAPL source after 25 years for two values of the intrinsic interface mass transfer coefficient (mm^{-2} hr^{-1}). Pore velocity = 10 m/yr, DNAPL is distributed across N = 10 spherical blobs, and source box dimensions = 1 x 1 x 1 m.

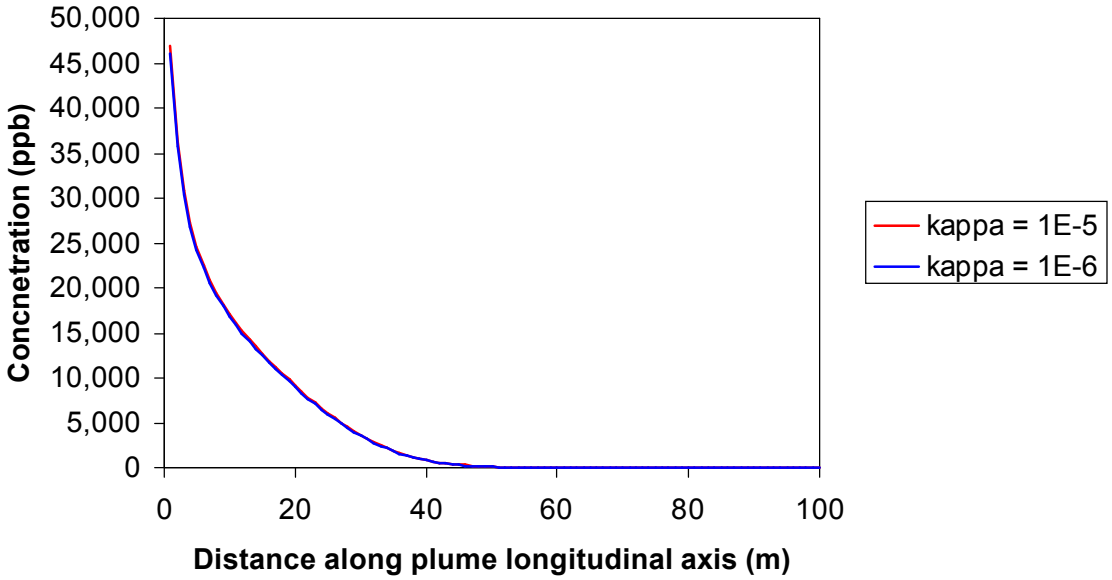

Figure 20. Longitudinal profiles of a groundwater TCE plume emanating from a 30-kg DNAPL source after 25 years for two values of the intrinsic interface mass transfer coefficient (mm^{-2} hr^{-1}). Pore velocity = 1 m/yr, DNAPL is distributed across N = 100 spherical blobs, and source box dimensions = 1 x 1 x 1 m.

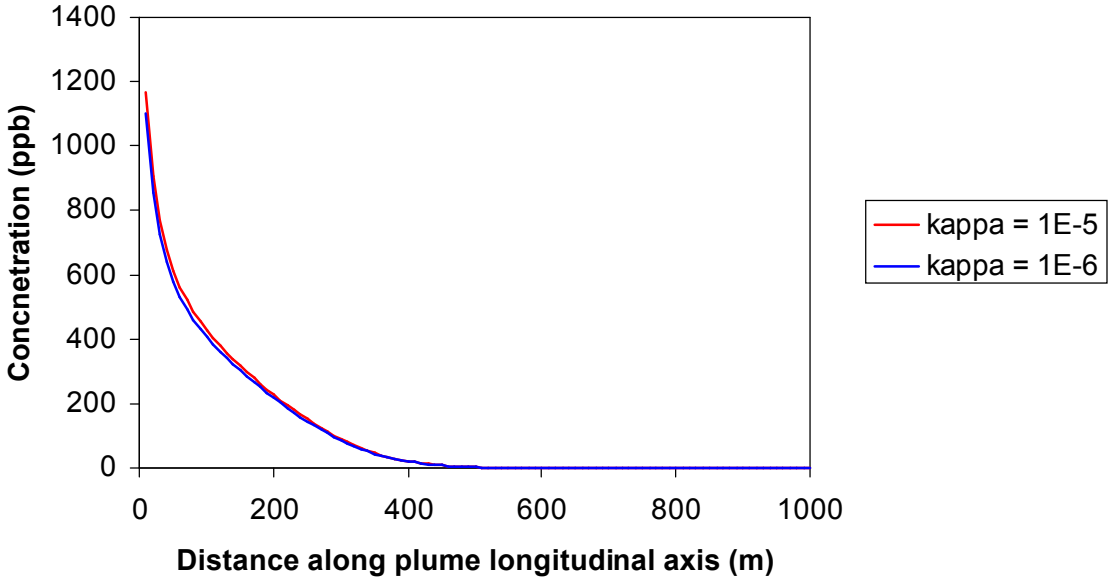

Figure 21. Longitudinal profiles of a groundwater TCE plume emanating from a 30-kg DNAPL source after 25 years for two values of the intrinsic interface mass transfer coefficient (mm^{-2} hr^{-1}). Pore velocity = 10 m/yr, DNAPL is distributed across N = 100 spherical blobs, and source box dimensions = 4 x 0.25 x 02.5 m (i.e., rectangular source box with major axis aligned with the direction of groundwater flow, presenting a comparatively small cross-sectional area).

Table 2. Implied TCE DNAPL dissolution times within the source box.

Pore velocity (m/yr)	N	Source box dimensions	κ (mm^{-2} hr^{-1})	Dissolution time (yrs)
10	100	1 x 1 x 1 m	1×10^{-5}	11.4
10	100	1 x 1 x 1 m	1×10^{-6}	16.4
10	10	1 x 1 x 1 m	1×10^{-5}	12.0
10	10	1 x 1 x 1 m	1×10^{-6}	22.8
10	100	4 x 0.5 x 0.5 m	1×10^{-5}	43.9
10	100	4 x 0.5 x 0.5 m	1×10^{-6}	49.1
1	100	1 x 1 x 1 m	1×10^{-5}	>50
1	100	1 x 1 x 1 m	1×10^{-6}	>50

These results indicate that the value of the DNAPL/water interface mass transfer coefficient is not necessarily the dominant factor in determining source longevity or plume morphology. In cases where the geometry of the source box (e.g., alignment of the longitudinal axis with the direction of groundwater flow), low groundwater velocity, or a high DNAPL blob specific surface value (e.g., the same DNAPL mass distributed over a large number of blobs rather than a small number), high concentrations of dissolved-phase TCE can develop within the source box, limiting subsequent dissolution. As such, the rate of advective transport of contaminants out of the source area, rather than the rate of DNAPL/water mass transfer, may be the rate-limiting step in influencing source longevity.

SUMMARY

Through a unique combination of experiments and simulations, this study has provided an unprecedented glimpse into mass transfer rate-limited dissolution phenomena of non-aqueous fluids on the pore scale. In particular, the detailed mathematical solution of the flow field surrounding a dissolving DNAPL blob – as described by the Navier Stokes equations – has permitted estimation of an intrinsic mass transfer coefficient for the TCE DNAPL/water interface, a quantity that had previously been intertwined with pore-scale geometry and mean pore velocity as a lumped parameter lacking a theoretical basis for upscaling. We have found that the mass transfer coefficient measured at the pore scale can be extended to the meso-scale (defined by several thousand mineral grains packed into various synthetic porous medium arrangements) using 3-D AMR numerical simulations on supercomputing platforms. At this scale, this mass transfer coefficient exhibits a very predictable dependence on grain size. Reactive transport experiments and simulations at this scale also suggest that the intrinsic mass transfer rate first quantified for an individual DNAPL blob in a Hele-Shaw scale can be applied under more complex conditions where aqueous phase reactions and mineral precipitation both affect DNAPL blob dissolution with time.

At larger scales, the computational and experimental approaches employed in this study are no longer practicable. Nevertheless, the intrinsic mass transfer relationship quantified at the pore-scale can be utilized directly as a parameter in groundwater plume models applied to the field scale. This allows an assessment of the overall significance of the mass transfer coefficient, in

comparison to other parameters such as groundwater velocity or geometry of the source area, on source longevity and plume morphology.

REFERENCES

Chatzis et al., *Soc. Pet. Eng. J.*, 24, 555-562, 1988.
Conrad et al., *J. Contam. Hydrol*., 58, 13-49, 2002.
Detwiler et al., *Water Resour. Res*., 35, 2605-17, 1999
Detwiler et al., *Water Resour. Res*.,36, 1611-25, 2000
Detwiler et al., *Water Resour. Res*.,37, 3115-29, 2001.
Fenwick and Blunt, *Adv. Water Resour*., 21(2), 121-143, 1998.
Glass et al., *Water Resour. Res*., 34, 3215-3234, 1998; 36, 3121-3137, 2001.
Gray et al., CRC, 1993.
Held and Celia, *Water Resour. Res*, 37, 539-549, 2001.
Jia et al., *J. Contam. Hydrol.* 35, 363-387, 1999.
Keller et al., U.S. EPA report, 2002.
Khachikian and Harmon, *Transp. in Porous Media*, 38, 3-28, 2000.
Nicholl et al., *Water Resour. Res*., 35, 3361-3373, 1999.
Parkhurst and Appelo Calculations; U. S. Geological Survey Water-Resources Investigations Report 99-4259, 2002.
Phillips, *Flow and Reactions in Permeable Rocks*, Cambridge University Press, 1991.
Wan et al., *Water Resour. Res*., 32, 1955-1964, 1996.
Wilson and Conrad, *Water Well Assoc*., Houston, Tex., 1984.
Wilson and Miller, *Proceedings of the American Society of Civil Engineers*, 104(4), 503-514, 1978.
Yan, Y.E., and F.W. Schwartz. *J. Contam. Hydrol.,* 37, 343-365, 1999.
Zhong et al., *Water. Resour. Res*., 37, 523-537, 2001.